www.sciencemag.org/cgi/content/full/science.aac9788/DC1

Supplementary Materials for

Direct sampling of electric-field vacuum fluctuations

C. Riek, D. V. Seletskiy, A. S. Moskalenko, J. F. Schmidt, P. Krauspe, S. Eckart, S. Eggert, G. Burkard, A. Leitenstorfer*

*Corresponding author. E-mail: alfred.leitenstorfer@uni-konstanz.de

Published 1 October 2015 on *Science* Express
DOI: 10.1126/science.aac9788

This PDF file includes:

Materials and Methods

Theoretical analysis and fundamental constants

The quantitative treatment of vacuum fluctuations and the electro-optic detection process has been carried out in SI units throughout this study. An elaborate theoretical derivation of the key expressions used in this paper may be found in Ref. (*30*) where electro-optic sampling is described as a nonlinear mixing process of quantized Laguerre-Gaussian modes. A dot on top of a variable denotes the temporal derivative, e.g. $\dot{x} \equiv \partial x/\partial t$. A bar above an observable, e.g. $\bar{E}$, indicates quantities averaged over the space-time volume probed by the gate pulse. Vectorial quantities are designated by bold symbols, e.g. **k**, **A**. Standard italic or Greek fonts are used for scalar quantities or to denote the absolute value of a vectorial quantity. The fundamental constants involved in our analysis are the velocity of light in vacuum $c \approx 3.00 \times 10^8$ m/s, permittivity of free space $\varepsilon_0 \approx 8.85 \times 10^{-12}$ As/(Vm), Planck's constant $h = 2\pi\hbar \approx 6.63 \times 10^{-34}$ Js and Boltzmann's constant $k_B \approx 1.38 \times 10^{-23}$ J/K.

Note that our derivation of Eq. (5) models the case of perfect impedance matching of the EOX to free space via e.g. a broadband anti-reflection coating. An identical result would be obtained when assuming perfectly reflecting crystal surfaces: in this case, one has to employ the operator for the electric field inside the medium where ε_0 is replaced by $\varepsilon\varepsilon_0 = n_0^2\varepsilon_0$ (*1*). Adjusting the mode density inside the dielectric to n_0L/c instead of L/c for free space then leads to the same expression as in Eq. (5). Our experiment with an uncoated crystal operates closer to the first case with 60% of the detected vacuum amplitude coupled in directly from free space and 40% originating from multiple reflections.

Generation of phase-locked mid-infrared transients and detection of the electric field

Our setup starts with an ultrabroadband Er:fiber source (*34*) ensuring excellent stability (Fig. S1). A modelocked laser oscillator provides a femtosecond pulse train at a repetition rate of 40 MHz. After a fiber-optic beam splitter, it seeds two parallel Er:fiber amplifiers. Every second pulse is selected in the pump branch by a fiber-coupled electro-optic modulator (EOM), reducing the repetition rate to 20 MHz. The amplifier output is compressed by a Si prism sequence and generates an ultrabroadband dispersive wave centered at a wavelength of 1.15 µm in a highly nonlinear fiber assembly. Dispersion compensation by an SF10 prism sequence results in a pulse duration of 7.2 fs. This pump is focused to a beam diameter of 16 µm at the exit surface of a lithium niobate crystal with a poling period of 29 µm. It produces a passively phase-locked multi-THz transient via quasi-phase-matched difference frequency mixing within the ultrabroad NIR spectrum. This pulse is collimated by an off-axis parabolic mirror (focal length $f_1 = 50$ mm) and passes a Ge filter to block residual NIR.

The second arm (probe) of our Er:fiber system lacks an EOM for pulse picking and the repetition rate remains at 40 MHz. The intensity envelope of vertically polarized sub-1.5-cycle pulses of a duration of $t_p = 5.8$ fs used for probing is shown in Fig. S2A, as measured with two-dimensional spectral shearing interferometry (*35*, *36*). Amplitude and

phase spectra of the probe are depicted in Fig. S2B as blue and red lines, respectively. The two branches are spatio-temporally overlapped by means of an optical delay stage and a silicon beam combiner. An electro-optic sensor is located in the focus of an off-axis parabolic mirror with f_2 = 25 mm. A $AgGaS_2$ crystal as thin as l = 30 μm serves for phase-matched electro-optic (EO) detection. The symmetry is such that an EO phase shift proportional to the co-propagating multi-THz field amplitude causes a change in the polarization state of the probe. This effect is analyzed with a quarter-wave plate and Wollaston polarizer. A differential photocurrent ΔI is detected on top of the overall photocurrent I with a pair of balanced InGaAs photodiodes and a radio-frequency lock-in amplifier (RFLA). In all experiments, $\Delta I/I$ is referenced to single-pulse readout by normalizing with the square-root of the lock-in bandwidth. Measuring at the Nyquist frequency of 20 MHz provides quantum-limited amplitude stability and timing jitter. We flush the setup with dry N_2 to avoid CO_2 and H_2O vibrational absorption bands.

Properties of $AgGaS_2$ electro-optic detector

$AgGaS_2$ belongs to the group of I-III-VI_2 semiconductors. Its chalcopyrite crystal structure emerges by uniaxially distorting the zincblende lattice common to many II-VI compounds and replacing the group-II atom by alternating Ag (group-I) and Ga (group-III) atoms, respectively. Negative uniaxial birefringence allows for type-II phase-matching in electro-optic detection. Optimally broadband conditions for signals centered around 70 THz and sampling with a probe carrier frequency of 255 THz occur under a phase-matching angle of Θ = 48°. This geometry allows exploiting a relatively long interaction length of l = 30 μm while keeping a full width at half maximum of the spectral response comparable to the center frequency.

The linear refractive index corresponding to our phase-matched situation amounts to n_0 = 2.40±0.01 (*37*). The absolute value of the purely electronic contribution to the clamped EO coefficient r_{41} was calculated to be 7.58 pm/V (*38*) in the dispersionless regime far from the bandgap. We can directly adopt this input since we read out our signals with a carrier frequency of 255 THz which is substantially below the interband resonance frequency of $AgGaS_2$ of 650 THz (bandgap of 2.7 eV). The large bandgap energy also ensures absence of two-photon absorption for the probe. On the other side, we can neglect the influence of ionic contributions to the nonlinearity since we drive the EOX with frequencies between 30 THz and 140 THz which are far above the highest TO phonon resonance in $AgGaS_2$ at 11 THz. Note that the unclamped electro-optic coefficient of r_{41} = 4.0 pm/V measured with electric fields in the acoustic frequency range (*39*) differs from the value relevant in our experiment since under those conditions microscopic lattice displacements and macroscopic electrostriction in combination with piezoelectricity take part in the nonlinear process. Their contributions are opposite in sign with respect to the purely electronic effect (*25, 38, 40*). Therefore, a larger nonlinearity results when driving the EOX far above any lattice and mechanical resonance frequencies as in our case.

Total frequency response $R(\Omega)$ of the system

A quantum theory (*30*) of our problem supports calculation of the frequency response function $R(\Omega)$ following the lines of a classical treatment in the frequency domain (*29*) where electro-optic detection is understood as a combination of sum- and difference frequency mixing of the multi-terahertz wave form at frequencies Ω within the ultrabroadband near-infrared probe spectrum. The finite intensity envelope of the probe results in a normalized frequency response given by the spectral autocorrelation of the probe electric field, as depicted in Fig. S3 for t_p = 5.8 fs (green line) and a probe stretched to t_p = 100 fs by detuning one of the SF10 prisms in the compressor stage (blue). A value approaching unity corresponds to the negligible influence of a finite probe temporal envelope which occurs under stationary conditions, i.e. at $\Omega = 0$. The 5.8 fs probe allows sampling of frequencies in excess of 100 THz while stretching to t_p = 100 fs leads to a collapse of the response into the few-terahertz regime. The relative amplitude response due to phase matching is depicted as a green line in Fig. S4A. Note that it effectively contains a product of phase-matching amplitudes due to sum- and difference frequency mixing which have to be present at the same time in order to allow for multi-THz quantum detection. A lower frequency cut-off at $\Omega/2\pi$ = 30 THz is caused by the onset of strong dispersion of $AgGaS_2$ when approaching the Reststrahlen band. This feature keeps our setup from sensing thermal fluctuations which occur at lower frequencies. Since the dispersion of the electro-optic coefficient may be safely omitted because we work far off all intrinsic resonances of $AgGaS_2$, multiplication of the phase-matching amplitude with the frequency response provided at the minimum probe duration of 5.8 fs (reproduced as a blue line in Fig. S4A) results in the full normalized amplitude response $R(\Omega)$ of our setup (blue line in Fig. S4B). The effective spectral bandwidth $\Delta\nu = \Delta\Omega/2\pi$ = 66 THz, center frequency $\nu_c = \Omega_c/2\pi$ = 67.5 and average amplitude response $R(\nu_c)$ = 0.41 (all indicated by the red square in Fig. S4B) are chosen such that when inserting them into Eqs. (5) and (6), the same result is obtained in Eq. (7) as compared to when the full frequency integral over $R(\Omega)$ would have been carried out in Eq. (4).

Transverse geometry of electro-optic quantum sampling

The transverse intensity profile in the focus of the probe beam exploited in our experiment is depicted in Fig. S5. Since the probe pulses emerge from a single-mode highly nonlinear fiber, they are very close to the theoretical limit of a fundamental Gaussian TEM_{00} mode. The standard spot radius w_0 used in paraxial theory of Gaussian beams is obtained from the full width at half maximum (FWHM) of the intensity by multiplication with $(2\ \ln 2)^{1/2} \approx 0.85$. Therefore, a FWHM of the probe beam of 5 μm corresponds to w_0 = 4.25 μm.

Ruling out spurious effects

It is important to exclude alternative explanations for the decreasing width of the readout distribution of the electro-optic field measurement when the probed space-time volume is expanded. First of all, the mean photon energy of

$h\nu_c = \hbar\Omega_c = 280$ meV >> $k_B T = 25$ meV keeps thermal mode occupation close to zero even at $T = 300$ K. The $AgGaS_2$ detector becomes inefficient at photon energies below 100 meV due to the onset of absorption and a lack of phase matching (see Fig. S4). In addition, stretching the probe pulse duration to 100 fs still provides a bandwidth of approximately 5 THz (see Fig. S3). Therefore, any low-frequency spurious signals that might e.g. arise at our RFLA reference of 20 MHz via piezoelectric coupling of thermal fluctuations would not lead to a differential effect with respect to probing with $t_p = 5.8$ fs. Absence of such effects has also been checked by comparing the probe noise level obtained at stretched space-time volume to the situation with the EOX removed. Influences due to phase-mismatched second-harmonic generation at the surfaces of the EOX or multi-photon absorption are ruled out by the fact that our sampling average power changes by less than 10^{-2} when altering the probe duration or moving the EOX out of focus. Measuring at this level of amplitude stability is enabled by the excellent noise performance of our femtosecond Er:fiber source. In addition, both processes would rather tend to generate the opposite effect as compared to the influence of the multi-THz vacuum due to a slight attenuation of amplitude fluctuations at the fundamental probe frequency expected with increasing intensity. Self-phase modulation of the 5.8 fs probe might lead to a minor broadening of the spectrum while conserving the total number of photons in each pulse. Nevertheless, this process is not yet discernible in the transmitted spectrum under the tightest focusing conditions $w_0 = 4.25$ μm and short length $l = 30$ μm of the EOX employed in this study. The broadband response of our photodiodes also avoids any direct influence on probe photon statistics by nonlinear spectral broadening. Nonlinear effects in the photodiodes themselves are excluded by stretching the probe pulses into the sub-picosecond regime during transmission through optical elements after the EOX and gentle focusing to a diameter of 60 μm. Maximum care has been taken for using clean optical surfaces and retaining the balance of the differential photodetector. Free-standing $AgGaS_2$ electro-optic crystals have been lapped and fine-polished in house, ultimately using SiO_2 nanoparticles of a diameter of 30 nm. Residual strain and traces of surface oxidation have subsequently been removed by thermal annealing of the EOX at 300 °C. Minute effects due to variations of Fresnel losses when moving the EOX out of focus have been accounted for by monitoring the transmitted probe power with a relative accuracy better than 10^{-3} and subsequent correction for the resulting change of noise-equivalent field when collecting the quantitative data set shown in Fig. 4. Note that our EOX would be expected not to generate terahertz amplitude itself in case of a purely zincblende-type specimen operated under maximally efficient orientation (*30*). However, we measure a maximum electric field amplitude of 1 V/cm from optical rectification when using a $AgGaS_2$ crystal identical to our electro-optic detector as an emitter and exciting it with NIR pulse characteristics analogous to the probe. Most likely, this effect is due to the lower symmetry of $AgGaS_2$ as compared to e.g. ZnTe in combination with the finite range of lateral wave vectors provided by the tight focusing. Considering the Fresnel reflections at the emitter and detector surfaces as well as some losses in the transmission system, we estimate a maximum THz amplitude of 4 V/cm that is generated inside the EOX. Owing to the small pulse-to-pulse relative intensity fluctuations in our probe beam of approximately 3×10^{-5}, a noise contribution from this process results that is more than four orders of magnitude lower than the vacuum field amplitude we detect.

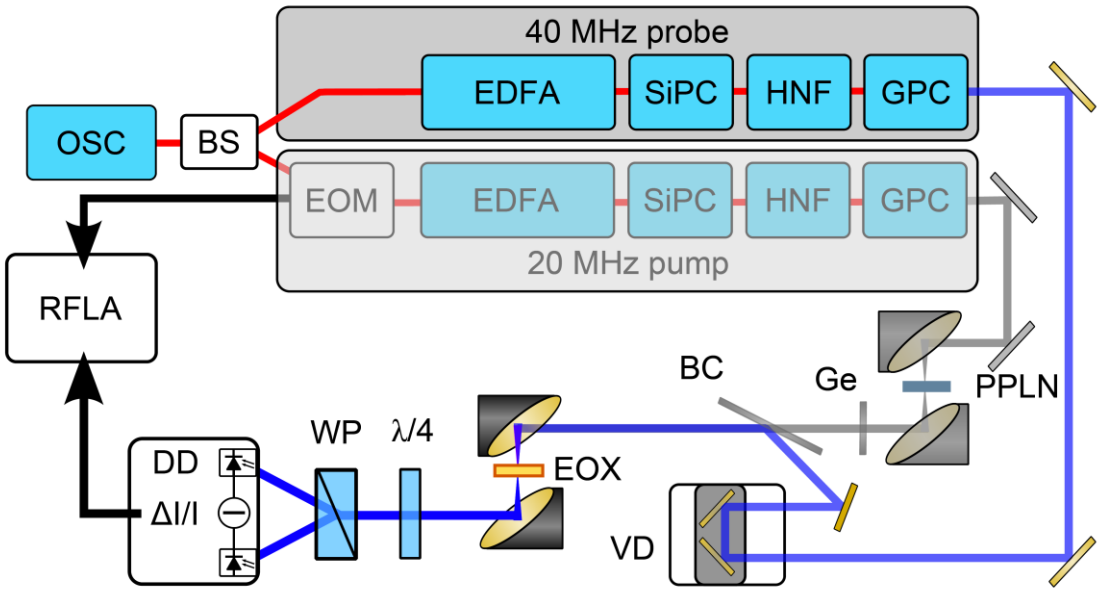

Fig. S1

Scheme of the experimental setup for measuring ultrabroadband classical electric field transients and the fluctuation amplitude of the multi-terahertz quantum vacuum. An Er:fiber modelocked oscillator (OSC, 40 MHz repetition rate) seeds two parallel femtosecond Er:fiber amplifiers (EDFA) after a fiber-optic beamsplitter (BS). In the pump branch, the pulse repetition rate is reduced to 20 MHz by an electro-optic modulator (EOM). SiPC: silicon prism sequences for compression of EDFA outputs. HNF: highly nonlinear germanosilicate fibers for generation of coherent supercontinua. GPC: SF10 prism compressors for HNF outputs. Setup for multi-terahertz electro-optic sampling: variable optical delay stage (VD), periodically-poled lithium niobate crystal (PPLN) for optical rectification of the pump, off-axis parabolic mirrors for achromatic collimation and focusing, germanium filter (Ge), silicon beam combiner (BC), $AgGaS_2$ electro-optic crystal (EOX), quarter wave plate (λ/4), Wollaston prism (WP), differential detector (DD) and radio-frequency lock-in amplifier (RFLA) referenced to the trigger signal for the EOM at 20 MHz. Classical electro-optic signal is obtained by the readout of the demodulated output of the RFLA versus the position of the delay stage. Quantum vacuum is analyzed after deactivating the pump branch (shaded).

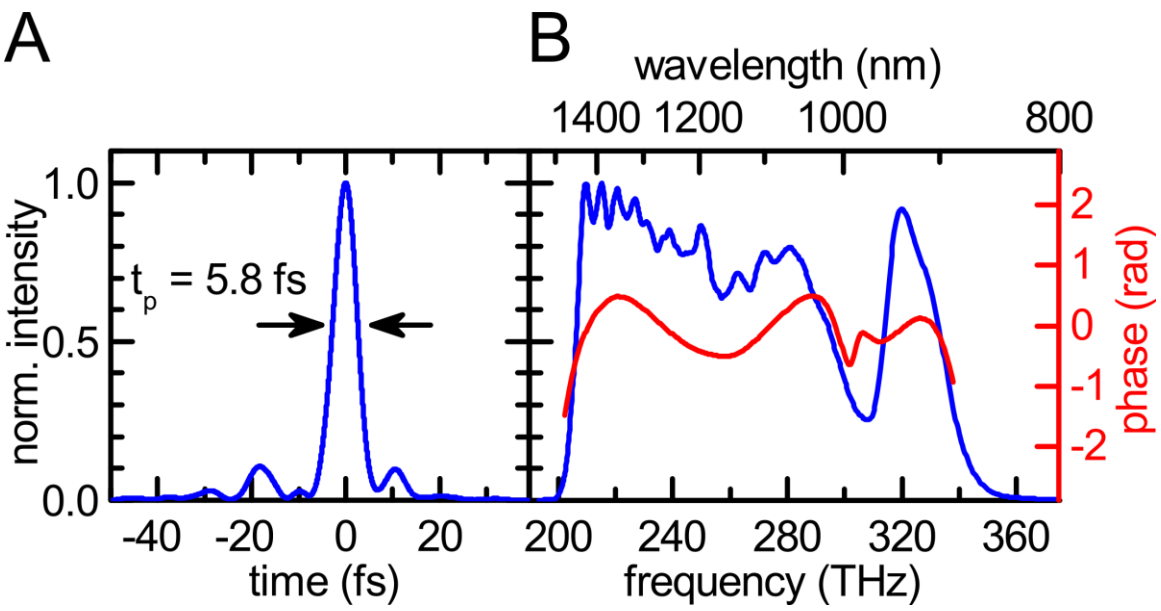

Fig. S2

Temporal and spectral characteristics of the 1.5-cycle near-infrared probe pulse as obtained by 2-dimensional shearing interferometry. (A) The temporal envelope of the intensity (blue line) indicates a full width at half maximum of 5.8 fs. (B) Intensity (blue) and phase (red) depicted versus frequency and wavelength, demonstrating a bandwidth of 140 THz and nearly transform-limited character of the unchirped wave packet.

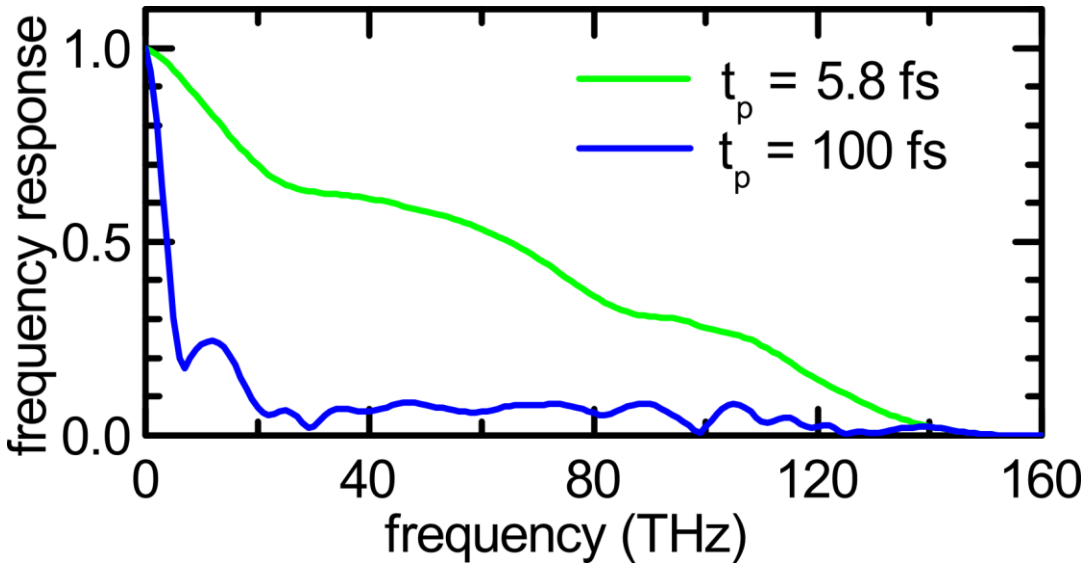

Fig. S3

Frequency response of the electro-optic detection system due to finite width of the temporal intensity envelope of the probe. The green line is calculated with the amplitude and phase spectra of the compressed 5.8 fs pulse from Fig. S2B. The blue line is obtained when adding the dispersion introduced by moving one SF10 prism in the compressor stage away from the optimum position by 900 μm. Some sensitivity remains at high frequencies due to temporal sub-structure that arises because of higher-order dispersion but most of the potential spectral response is now concentrated below 5 THz due to stretching of the pulse to a FWHM of the intensity envelope of approximately 100 fs.

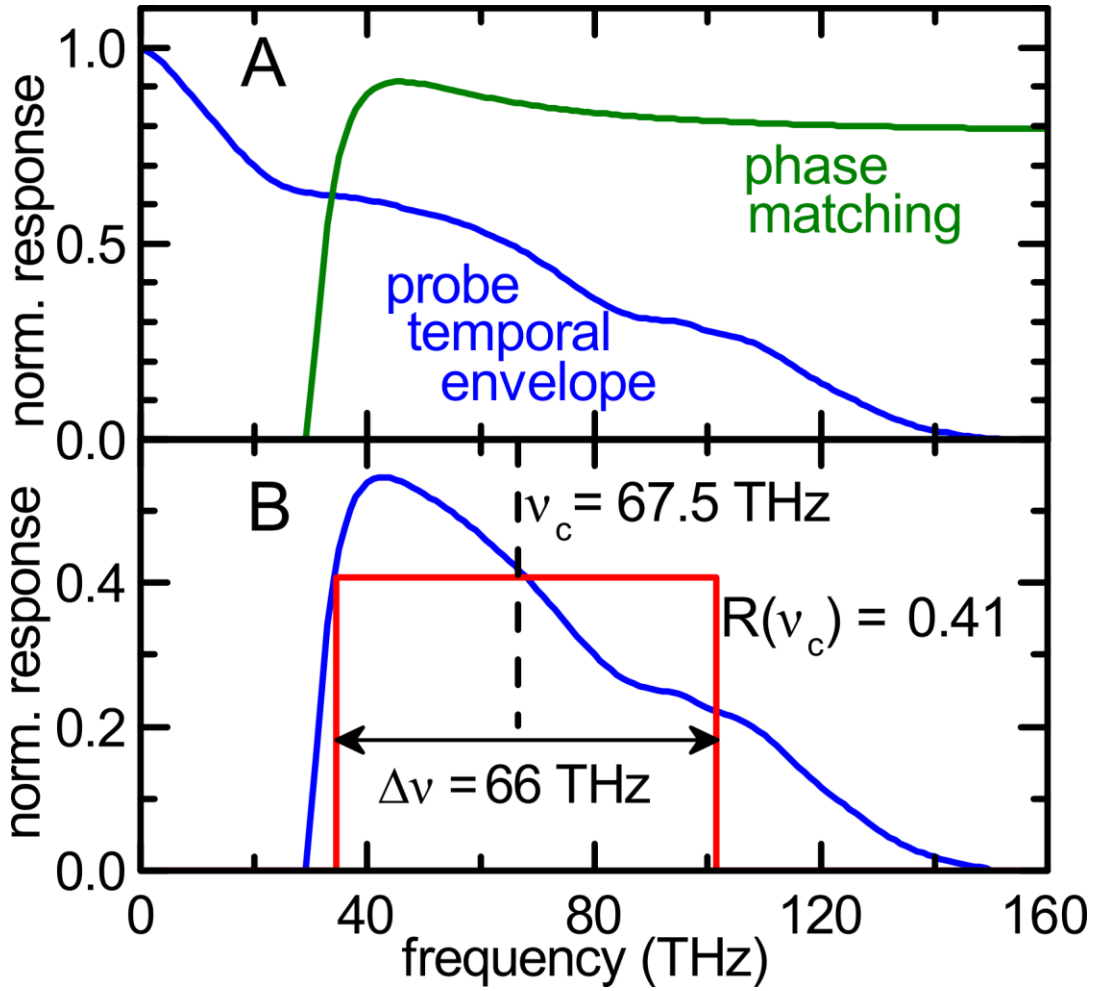

Fig. S4

(A) Frequency response provided by the 5.8 fs probe (blue line) and calculated for the phase-matching conditions inside the electro-optic crystal (green line). Note that the phase-matching never fully approaches unity because our crystal is optimized for maximum bandwidth and the requirement for simultaneous phase matching of both sum and difference frequency generation of the multi-THz signal within the ultrabroadband near-infrared probe. **(B)** Complete amplitude response function of the entire system, as obtained via multiplication of the two contributions shown in (A). The center frequency ν_c, spectral bandwidth $\Delta\nu$ and average amplitude response $R(\nu_c)$ are chosen such that the full frequency integrals occurring in the equations for the vacuum amplitude and noise-equivalent field are parameterized correctly.

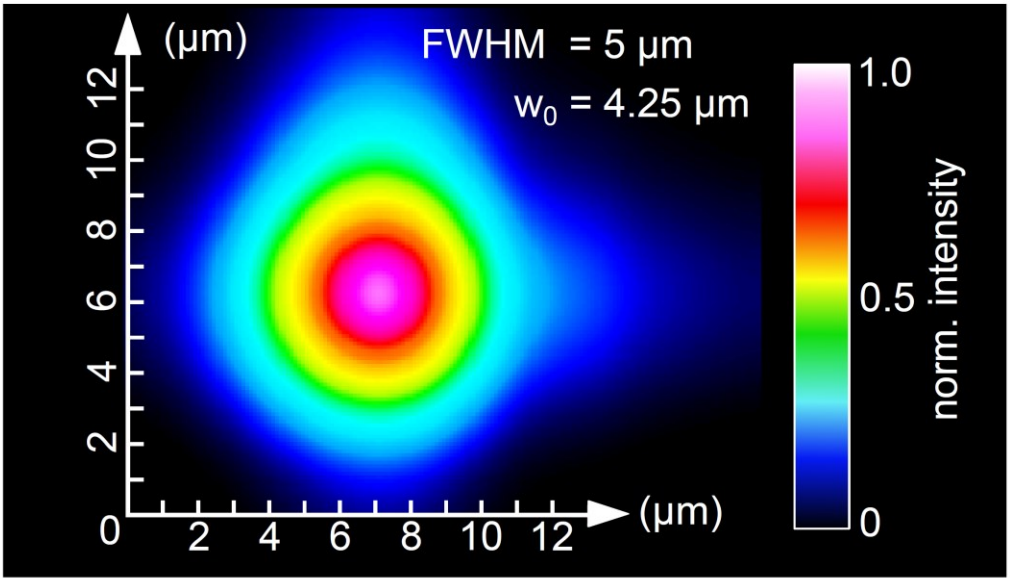

Fig. S5

Confocal intensity profile of the probe beam, as measured with a commercial slit-scanning device. The same focusing geometry has been used for all experiments discussed in this paper.